Article

Synthesis and Characterization of Carbon-Based Quantum Dots and Doped Derivatives for Improved Andrographolide's Hydrophilicity in Drug Delivery Platforms

Nataniel Medina-Berríos,* Wenndy Pantoja-Romero, Alexis Lavín Flores, Sebastián C. Díaz Vélez, Anna C. Martínez Guadalupe, Mariana T. Torres Mulero, Kim Kisslinger, Magaly Martínez-Ferrer, Gerardo Morell, and Brad R. Weiner

Cite This: *ACS Omega* 2024, 9, 12575−12584

Read Online

| ACCESS | | Metrics & More | | Article Recommendations | | SI Supporting Information |

ABSTRACT: Carbon-based quantum dots (CBQDs), sulfur-doped carbon-based quantum dots (S-CBQDs), and nitrogen-doped carbon-based quantum dots (N-CBQDs) have strong potential for drug delivery platforms. They were conjugated with andrographolide, a well-known hydrophobic drug, to study the concomitant changes in hydrophilicity. The interactions between these nanomaterials and the drug were studied by characterizing the optical and structural properties of the nanoparticles before and after coupling with the drug. It was found that the interaction of the drug with these nanomaterials produced noticeable changes in their optical and structural properties. Moreover, the partition coefficient for the nanocomposites was determined by NMR. The results indicate that conjugating the drug with the nanoparticles significantly enhanced its affinity for the aqueous phase, from 2.632 to 0.1117, thereby opening the possibility of using this approach for developing an effective drug delivery platform for this hydrophobic drug.
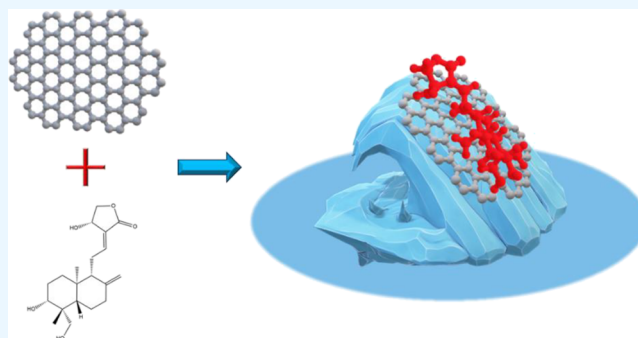
1. INTRODUCTION

Andrographolide (ADG), a bicyclic diterpene-*g*-lactone found in the plant *Andrographis Paniculata*, possesses multidimensional therapeutic potential, e.g. anti-inflammatory, anti-HIV, and anticancer properties.[1] Among its anticancer properties, it has been shown that ADG sensitizes prostate cancer cells to tumor necrosis factor-related apoptosis-inducing ligand[2] (TRAIL)-induced apoptosis.[3] However, ADG is known to have low solubility in water (74 μg/mL), which limits its therapeutic use because of low bioavailability when administered orally.[4] Andrographolide's bioavailability, the proportion of a drug that reaches the systemic circulation in its active form[5], has been found to range from 1 to 2%.[6,7] As a result, a variety of methods have been studied to increase this bioavailability, as well as improve the solubility of ADG in water.[8−10]

There are a variety of methods to improve the solubility, including nanoparticles (NPs), liposomes, nanoemulsions (NE) or microemulsions (ME), cyclodextrins, microspheres, solid dispersions, and manipulation of the particle size distribution. Cyclodextrins (CDs) are cyclic oligosaccharides with a hydrophilic outer shell and a lipophilic cavity in the center. The α, β, and γ are the three most used forms of CDs.[11] Ren et al.[12] prepared an AND/HP-β-CD complex by solvent evaporation and characterized it by the phase solubility method. It showed that the solubility of ADG increased linearly as a function of HP-β-CD concentration, resulting in an A_L-type phase solubility diagram. However, the parenteral administration of cyclodextrins can cause nephrotoxicity and hemolysis.[13] In another study, an oil-in-water (O/W) ME loaded with ADG was developed by using isopropyl myristate, Tween 80, ethanol, and water. The solubility of ADG in this (O/W) ME was 8.02 mg/mL, 2 orders of magnitude higher than the solubility of ADG in water (74 μg/mL).[14] Nonetheless, a suitable ADG carrier/delivery system has not yet been developed.

Nanoparticle-based drug delivery systems have shown promise in cancer treatments because they increase drug performance via improved pharmacokinetics and biodistribution characteristics.[15] Improvement of drug delivery is possible because nanoparticle-based carriers can be adjusted to meet
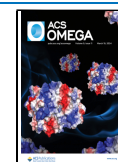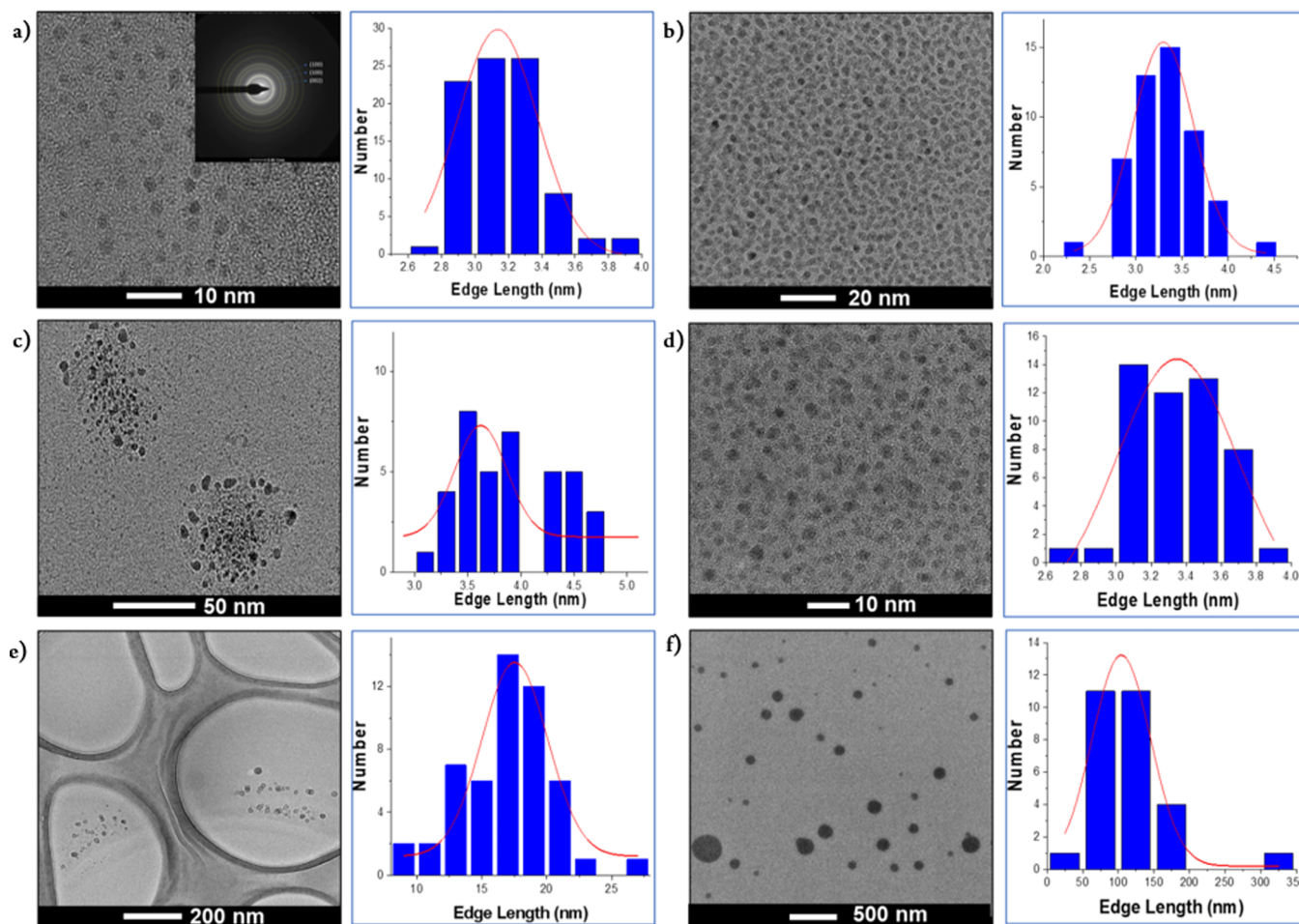
Figure 1. HR-TEM image and histogram (inset) of (a) CBQDs, (b) N-CBQDs, (c) S-CBQDs, and (d) CBQDs-ADG.

specific needs, such as spatial and temporal control of drug delivery and release, which improves medication efficacy. Nanocarriers may be designed to actively bind to specific cells by attaching targeting agents, such as ligands, to the surface of the nanoparticle. Most nanoparticles are engulfed through endocytosis and travel to endo/lysosomal compartments, which contain an acidic environment (pH = 4.5−5.5) compared to the extracellular environment (pH = 7.4). Since some cancerous cells have acidic properties, pH can act as an internal parameter for the design of a drug delivery system that may release drugs inside tumor cells, resulting in a significant improvement in the drug's bioavailability.[16] Carbon Based Quantum Dots (CBQDs) are zero-dimensional nanoparticles defined as graphene sheets with lateral dimensions less than 100 nm and thickness of fewer than 10 layers.[17] They have applications in optoelectronics, organic photovoltaics, electronic devices, catalysts, electrochemistry, ion sensing, and bioimaging.[18] CBQDs exhibit size-dependent luminescence[19], high photo/pH-stability, high quantum efficiency, and chemical inertness compared to semiconducting quantum dots.[20−22] Due to these properties, CBQDs are excellent candidates as multifunctional drug delivery platforms.[23−26] Nonmetal heteroatom doping with atoms of similar size to carbon to produce doped CBQDs (D-CBDQs) has been used as a strategy to tailor the properties of the particles by changing their electronic structure. This similarity in size to carbon atoms produces uniform doping and structural defects.[27] Compared with undoped CBQDs, doped-CBQDs with highly

electronegative atoms (e.g., N and S) usually cause blue-shifted emission; however, those doped with atoms of low electronegativity (like P, B, and Se) result in a red-shifted emission.[27] These changes in λ_{max} of the luminescence toward the blue or red of the visible spectra occur because nonmetal heteroatom doping at specific sites can introduce more defect states and energy levels. This, in turn, alters the band gap of the D-CBQDs and produces strong fluorescence due to quantum confinement and edge effects.[28]

CBQDs can act as carrier probes for the therapy of cancer cells. In past reports, Doxorubicin (DOX) has been successfully loaded onto CBQDs as a trackable pH-sensitive biocompatible nanoparticle drug delivery system[16], and further insights into CBQDs for DOX delivery have been studied in loading capacity, cytotoxicity on MCF-7 breast cancer cells, and drug conjugation characterizations.[29]

A molecular dynamics simulation and free energy calculation study modeled the drug delivery process through the cell membrane using CBQDs of different sizes using doxorubicin and deoxyadenosine as model drugs.[30] The results suggest that the drug delivery process to the cell assisted by CBQDs involves a reduction of translocation-free energy permeating into the cell membrane. Due to the strong interaction between lipids and the CBQDs, the drugs were likely stabilized in the lipid membrane. The decrease in the translocation-free energy in the permeation process is thought to be because the CBQDs may protect the polar area of the drug from interactions with the hydrophilic heads of the lipids.[30] These properties of

CBQDs are the basis of the work reported here, in which nanoparticles are investigated as potential drug delivery platforms to help solubilize ADG in water.

An important initial step in the assessment of a nanoparticle for drug delivery is understanding the hydrophilicity of the conjugated drug nanoparticle system. The partition coefficient between 1-octanol and water (log P) is the common way of measuring the lipophilicity of a compound of pharmaceutical interest. In addition to the log P, there is the distribution coefficient (log D), which describes the lipophilicity of ionizable compounds. If the compound is not ionizable, log P and log D should be around the same value.[31] The higher the value, the more lipophilic the molecule is.[32] Since ADG has a high reported log P (2.632 ± 0.135)[33] and a log D at pH 7.4 of 1.4,[34] it is an ionizable molecule that is considered lipophilic. The log P may also serve as a comparison of the hydrophilicity of ADG before and after it has been modified or loaded into a drug delivery system. Nuclear magnetic resonance spectroscopy (NMR) has been previously used to determine this log P value in many molecules.[35−37] This method is particularly useful since it utilizes a sensitive technique and enables the processing of many samples in a short period of time with a small amount of sample. This procedure enabled us to assess the changes in ADG's log P when coupled with the CBQDs and D-CBQDs. Literature results of ADG solubility improvement sometimes mention the log P of the drug and/or the nanosystem alone but not how it changes after drug loading is done.[38−41] The General Solubility Equation (GSE) is a reliable method for predicting the molar aqueous solubility (S_w) for nonelectrolytes[42] and helps to establish possible trends with its estimates. To the best of our knowledge, this article shows the first measurement and comparison of the log P of a nanoformulation for ADG after drug loading versus the value of the drug alone.

2. RESULTS AND DISCUSSION

2.1. Transmission Electron Microscopy (TEM). The morphologies of CBQDs, N-CBQDs, and S-CBQDs were characterized using HR-TEM (Figure 1) As illustrated in the TEM images, the CBQDs show a monodisperse and spherical distribution with an average diameter of 3.2 ± 0.1 nm (Figure 1a). The doped N-CBQD nanocomposites (Figure 1b) are dispersed and have a uniform morphology with an average edge length of 3.3 ± 0.1 nm. Nitrogen's atomic radius is less than the size of the carbon atom, which is consistent with nitrogen doping not influencing the interplanar distance as shown in the XRD patterns (Figure 2). The TEM images of S-CBQDs nanocomposites show nonhomogeneous morphologies with an average diameter of 4.0 ± 0.1 nm. The sulfur atom is larger than N and C and may influence the size of the nanocomposite (Figure 1c). The small size of CBQDs may be attributed to the fact that when synthesizing the CBQDs at pHs lower than 10, the presence of hydroxyl groups hinders the aggregation of the carbon nanoparticles.[43] The coupling of ADG in hybrid composites denotes an increased size associated with the presence of the drug. The average in CBQDs -ADG is 3.6 ± 0.1 nm due to the same planar coupling of the ADG (Figure 1d), and the average diameters of N-CBQDs-ADG and S-CBQDs-ADG were 17.5 ± 0.4 and 125 ± 0.8 nm, respectively (Figure 1e,f). The drug coupling caused a noticeable size distribution change.

The elemental studies with EDS mapping confirm the coupling with N, S, and ADG in the CBQDs sheets (Figures
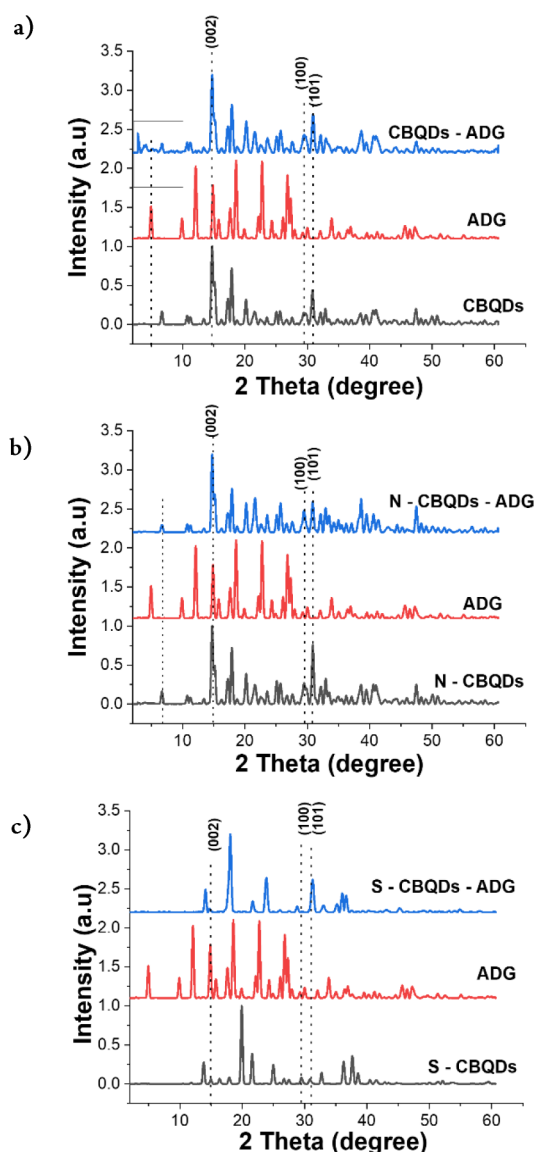

Figure 2. XRD pattern comparison of (a) CBQDs-ADG, ADG, and CBQDs, (b) NCBQDs-ADG, ADG, and NCBQDs, and (c) SCBQDs-ADG, ADG, and SCBQDs.

S1−S6). The selected area electron diffraction (SAED) patterns of CBQD represent the characteristic graphite planes (002), (100), and (101) (Figure S7). The shifted peaks and broadness as compared with graphite/CBQDs patterns are attributable to the quantum dots' small size and high crystallinity (Figure S7).[44−46] The high crystallization degree of GQDs suggests their high thermal stability.[47]

2.2. Powder X-ray Diffraction Studies. The crystal structure was studied by PXRD patterns of the synthesized CBQDs nanocomposites and the hybrid with ADG. Figure 2 shows a comparison of CBQD, ADG, and doped-CBQD-ADG. It is noted that the CBQD has the characteristic graphite planes (002), (100), and (101), whereas ADG presents its characteristic planes (002), (100), and (012) at 10°, 11.9°, and 15°, respectively. However, CBQD-ADG presents new peaks in the region from 0° to 10°, also with characteristic graphite planes. It is worth noting that this can be attributed to the form in which the drug is coupled to the CBQD, generating new planes in the XRD (Figure 2a). In addition, doping CBQD

with a hydrophobic drug like ADG most likely creates polar functional groups that are able to interact with the functional groups of ADG through electrostatic, H-bonding, and/or $\pi-\pi$ stacking interactions. Such interactions increase the adsorption energy of the drug on the carrier surface. It can be seen in N-CBQD-ADG and S-CBQD-ADG XRD profiles (Figure 2b, c) that the characteristic signals from ADG are suppressed. This can be explained by the ADG arranged in a parallel orientation with respect to the doped-CBQDs' surface.

2.3. NMR Studies for Interaction of ADG with CBQDs and D-CBQDs.
^{1}H and ^{13}C NMR methods were used to characterize and compare CBQDs, doped-CBQDs, and the starting reagents such as CA and 3-MPA (Figures S8−S15). New signals were observed in both ^{1}H NMR and ^{13}C NMR spectra when comparing the CBQDs and doped-CBQDs with CA, particularly around 1.5−3.5 and 5.5−6.0 ppm in the ^{1}H NMR spectra and around 80 and 165−180 ppm in the ^{13}C NMR spectra (Figure 3). The ^{1}H NMR signals around 1.5−2.6

Figure 3. (a) Stacked ^{13}C NMR of CBQDs and (b) citric acid in D$_2$O.

ppm in the products are consistent with Ph−CH$_2$−CH$_3$, a group that is not present in CA. The ^{13}C NMR signals around 120−140 ppm indicate the formation and presence of aromatic compounds in all the products, and those around 180 ppm present in both the reactants and the products are consistent with carboxylic acids. When 3-MPA acid was compared to the S-CBQDs, none of the reactant signals were observed in both ^{1}H NMR and ^{13}C NMR, indicating its consumption during the reaction and its absence in the product. N-CBQDs were not compared with ammonium chloride since the protons in ammonium chloride do not appear for a ^{1}H NMR spectrum in D$_2$O, due to rapid H/D exchange, and it possesses no carbons for a ^{13}C NMR spectrum. It was determined that there were no reactive residues present in the synthesized products after the purification process.

New signals and splitting patterns were observed between the CBQDs and the doped-CBQDs. When comparing the CBQDs with the S-CBQDs (Figures S9, S10, S13, and S14), an upfield shift was observed in both the ^{13}C NMR and ^{1}H NMR spectra. This shift was likely due to the S atom being less electronegative than C, creating a shielding effect.[48,49] In the ^{1}H NMR spectra, a new signal was observed around 7.27 ppm, indicative of a benzothiophene group. In the ^{13}C NMR spectra, new signals were observed at around 15−40 ppm, consistent with the formation of thioesters. There was a change in splitting patterns for the signals around 130 ppm, regions where benzothiophenes and phenanthrene-like groups signals are found. A different splitting pattern was observed around 6.52 ppm, most likely caused by the integration of a pyrrole group, known to happen in N-CBQDs.[50−52] In the ^{13}C NMR spectra, a different splitting pattern was observed around 40 ppm, the characteristic of amines.[53]

^{1}H and ^{13}C NMR analyses were done to assess the coupling between the CBQDs and D-CBQDs with ADG. Signals observed when comparing the CBQDs and D-CBQDs spectra with the CBQD-ADG and D-CBQD-ADG loaded spectra in both ^{1}H and ^{13}C NMR spectra confirmed the ADG loading (Figures S17−S19 and S21−S23). CBQD-ADG's ^{1}H NMR and ^{13}C NMR spectra were compared with CBQD's and
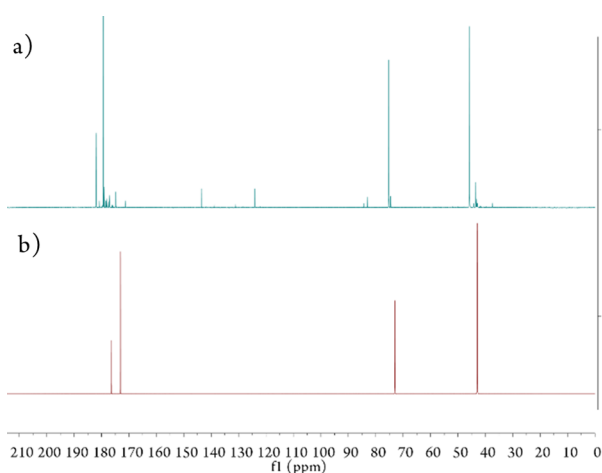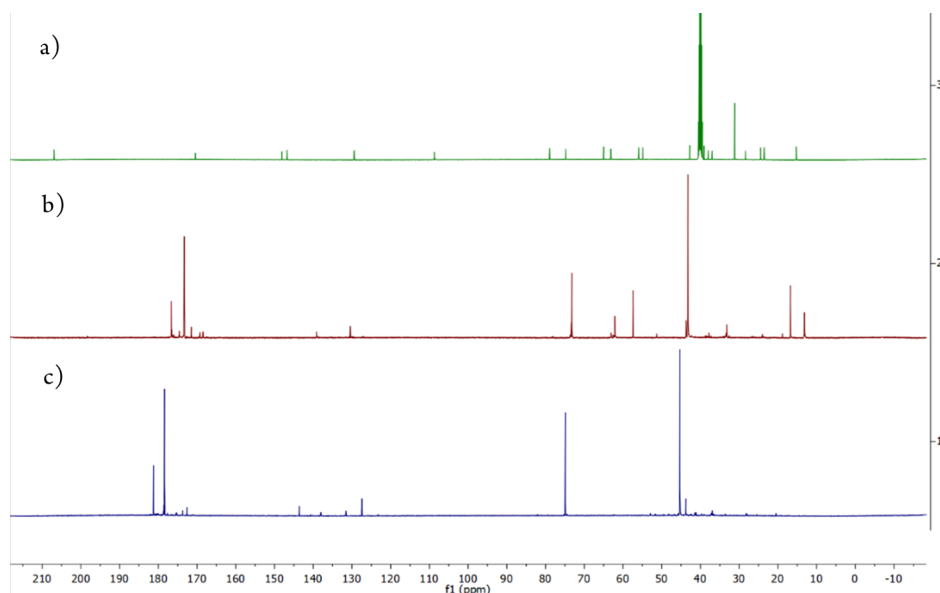

Figure 4. Stacked ^{13}C NMR of (a) andrographolide in DMSO-d_6, (b) SCBQD-ADG in D$_2$O, and (c) S-CBQDs in D$_2$O.

ADG's spectra (Figures S9, S10, S11, S13, S14, S15, and S16–S23). In the ^{1}H NMR spectra, shifts and splitting pattern changes were observed around 0.65–0.99 ppm; these two signals were present in ADG and CBQD spectra, respectively. Other shifts were observed around 1.77 ppm, a signal present in ADG spectra, and 6.28 ppm, a signal present in CBQD spectra. New signals were observed on CBQD-ADG's ^{1}H NMR around 8.40–8.61 ppm, indicative of aromatic groups. In the ^{13}C NMR spectra, new signals were observed at around 16.85 and 57.45 ppm. The rest of the signals observed correspond to the CBQDs. The changes in signals observed from both starting compounds in CBQD-ADG suggest the successful loading of ADG onto CBQDs.

The ^{1}H NMR and ^{13}C NMR spectra for N-CBQD-ADG were compared with the ^{1}H NMR and ^{13}C NMR spectra for N-CBQDs and ADG (Figures S19, S23, S11, S15, S16, and S20). New signals were observed around 0.98 3.27, 3.64, and 3.95 ppm. Changes in splitting patterns were observed around 1.10, 1.17, 3.43, 3.69, and 4.13 ppm, while shifts were observed around 1.17 and 5.64 ppm when compared with the ^{1}H NMR spectra for N-CBQDs. Splitting pattern changes were observed around 3.33 and 3.58 ppm, while shifts were observed around 8.38 ppm when compared with the ^{1}H NMR spectra of ADG. When comparing N-CBQD-ADG and ADG ^{13}C NMR spectra a shift was observed around 16.80 ppm, and new signals were observed around 57.43 ppm.

The ^{1}H NMR and ^{13}C NMR spectra for SCBQD-ADG were compared with the ^{1}H NMR and ^{13}C NMR spectra for S-CBQDs and ADG (Figures S18, S22, S10, S14, S16, and S2). For the ^{1}H NMR spectra of S-CBQDs, new signals were observed around 6.26, 6.73, 6.89, 7.07, 7.17, and 8.11 ppm. Shifts were observed around 0.04, 2.85, and 5.77 pm. When compared with the ^{1}H NMR spectra of ADG, a shift was observed around 5.77 ppm. Upon comparison of S-CBQD-ADG, S-CBQD, and ADG ^{3}C NMR spectra, new signals were observed around 13.14, 18.81, 139.07, 169.30, 176.67, and 198.44 ppm. Shifts were observed around 33.18, 43.21, 73.22, and 168.53 ppm when comparing with S-CBQD. ^{13}C NMR spectra and shifts around 62.10, 63.09, and 130.48 ppm were observed when comparing with ADG ^{13}C NMR spectra (Figure 4).

The presence of CBQD and DCBQD signals along with ADG signals in the CBQD-ADG and D-CBQD-ADG ^{1}H NMR and ^{13}C NMR spectra indicate the successful loading of ADG onto the quantum dots. The change in splitting pattern, the appearance of new signals, and the disappearance of certain signals evidence the coupling interaction between ADG and the CBQDs and D-CBQDs.

2.4. Partition Coefficient and GSE Results. The NMR log P measurements were done in triplicate and reported as an average with the standard deviation. Figure 5 shows an example of an NMR partition coefficient test using a selected signal normalized to the D$_2$O peak. Results are summarized in Table 1. ADG's results showed to be closer to the documented log D value (1.4 at pH 7.4). Coupling with CBQDs and D-CBQDs showed a significant decrease in lipophilicity. CBQDs showed the most improvement in solubilizing ADG, followed by S-CBQD and finally N-CBQD. The differences in performance in solubilizing ADG between the doped and undoped nanoparticles are deduced to be because of the differences in surface defects.

Table 2 summarizes the improvements in ADG's hydrophilicity in terms of concentration, while Table 3 shows GSE
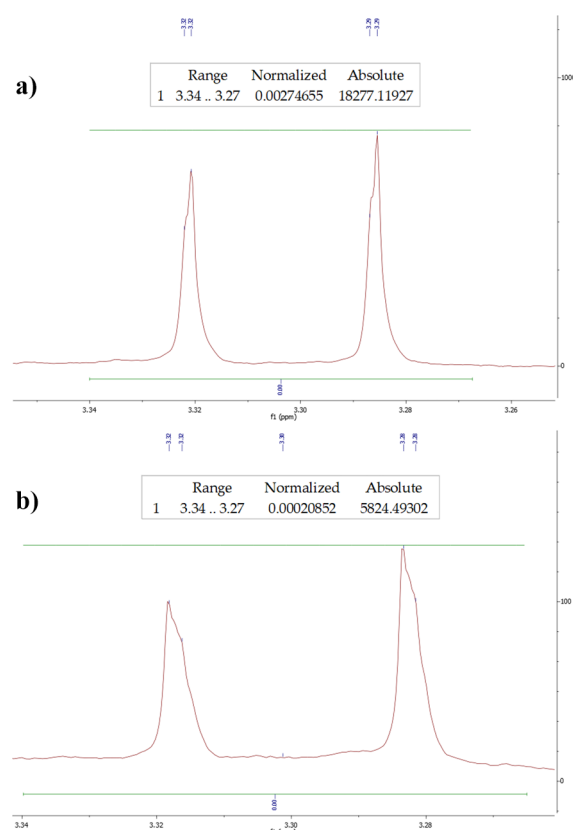

Figure 5. Example of an NMR partition coefficient test using a selected signal normalized to the D$_2$O peak. Corresponds to Replica 3 in Table 1. (A) ADG in D$_2$O and (B) ADG in D$_2$O after 1-octanol addition and 1 h of equilibrium.

Table 1. Results for Log P Tests by the NMR Method

material	$\overline{x}$	SD
ADG	1.1064	0.0189
CBQD	0.1927	0.0262
CBQD-ADG	0.1117	0.0513
S-CBQD	−0.6138	0.1047
SCBQD-ADG	0.2142	0.4029
N-CBQD	0.7594	0.1584
NCBQD-ADG	0.7775	0.0495

Table 2. Results for Solubility Improvement in Terms of μg/mL Based on a Starting Concentration of 8.76 μg/mL of ADG

material	$\overline{x}$ (μg/mL)	SD	ADG left in D$_2$O (%)
ADG	0.64	0.03	7.26
CBQD-ADG	3.82	0.25	43.62
SCBQD-ADG	3.45	1.80	39.38
NCBQD-ADG	1.26	0.12	14.34

Table 3. Results for GSE Calculations

material	log P	S_w (μg/mL)	ratio
ADG	2.632[33]	22.52	N/A
CBQD-ADG	0.1117	7463.32	331.36
SCBQD-ADG	0.2142	5894.30	261.70
NCBQD-ADG	0.7775	1611.14	71.53

results to estimate water solubility. It can be noted that CBQD-ADG and SCBQD-ADG nanocomposites have a higher average concentration of ADG related to that of NCBQD-ADG left in water. GSE results show that there was over 331.36 times increase in water solubility for ADG with CBQDs, 261.70 times with S-CBQDs, and 71.53 times with N-CBQDs when compared with ADG's S_w using its log P from literature for the GSE.[33] Yen et al. reported the solubility of ADG in α-tocopherol as 2.51 ± 0.25 mg/mL, using nanoemulsion as a strategy for improving the oral bioavailability and solubility for ADG.[54] On the other hand, Du et al.[14] used a microemulsion to improve the solubility of ADG, obtaining a solubility value of 8.02 mg/mL. Compared to the results mentioned above to improve the solubility of ADG, the results herein show a comparable increase in solubility in relation to previous ME results without altering ADG's structure, nor isolating ADG from water. It can be hypothesized that the increase in ADG solubility in this work was caused by the coupling of the drug with CBQDs and D-CBQDs mainly through the $\pi-\pi$ interactions forming soluble nanocomposites.

2.5. Fluorescence, UV−vis, and FTIR. To study the spectroscopic properties of the CBQDs and D-CBQDs and their nanocomposites, UV−vis absorption and FLU spectra with different wavelengths were carried out in water and ethanol. UV−vis spectra show that CBQDs present a strong band at 254 nm (Figure S24 left), indicating a size uniformity of sp^2 clusters. Therefore, mostly $\pi-\pi$ bonds were formed during the pyrolysis or carbonization, demonstrating that there is a considerable π-network. However, N-CBQDs show two absorption bands at 254 and 330 nm (Figure S4 left). The absorption band at 330 nm is attributed to the n−π* transition of the C−N[55] It further indicates that the nitrogen element is successfully doped into the structure of N-CBQDs. S-CBQDs show an absorption band at 254 nm just as N-CBQDs, and CBQDs also due to the $\pi \rightarrow \pi$* transition of the surface states[56]. The use of ethanol for ADG was necessary due to its low solubility in water, but the CBQDs-ADG and D-CBQDs-ADG composites were completely soluble in water. It was observed that the association of ADG on the CBQDs and D-CBQDs produced a shift in the peaks and the appearance of a new shoulder peak distinct from the absorption of pure ADG as well as the D-CBQDs, as shown in Figure S24 (right).

The fluorescence (FLU) spectra were obtained, as shown in Figure S25. The CBQDs and D-CBQDs were exposed to their corresponding excitation and emission values of λ_{max} (Table 4). The peaks marked with arrows in Figure S25 correspond to Rayleigh peaks. Doping CBQDs with S and N atoms could effectively modulate the band gap and electronic density of CBQDs, leading to a significant fluorescence blue shift. The

Table 4. Excitation and Emission Wavelengths of CBQDs, D-CBQDs, and Loaded Products

material	excitation λ_{max} (nm)	emission λ (nm)	
ADG	302	337	371
CBQD	370	462	882
CBQD-ADG	380	484	
N-CBQD	367	435	851
N-CBQD-ADG	381	450	853
S-CBQD	354	438	851
S-CBQD-ADG	351	439	852

FLU of CBQDs is subject to the influence of surface functional groups, which are observed in two bands at 370 and 462 nm (Figure S25a).[57] However, CBQD-ADG has strong excitation spectra compared to bare CBQD and ADG, which are excited at 380 nm with an emission wavelength of 484 nm. On the other hand, N-CBQDs have maximum excitation intensity at 367 nm with an emission wavelength of 435 nm which has been attributed to uniformity in size and emission sites of sp^2 clusters in the N-CBQDs.[58] N-CBQD-ADG, showed strong excitation spectra at 381 nm, a 14 nm shift from lone N-CBQDs, and an emission shift of 15 nm at 450 nm. S-CBQDs showed a well-defined emission band at 438 nm[59]. In the case of S-CBQD-ADG, no significant shifts were observed in the excitation and emission wavelengths.

CBQDs, doped-CBQDs, and their loadings were characterized by FT-IR to investigate any spectral changes of the functional groups after the coupling, and to corroborate the presence of ADG in the samples without losing their chemical integrity. An FT-IR spectra comparison of CBQD, N-CBQD, and S-CBQD with their characteristic starting materials was carried out (Figure S26). It can be observed that the peaks at 1212, and 1390 cm^{-1} correspond to C−S and C−N stretching in S-CBQDs, and N-CBQDs, respectively, while the peak 3100−3500 cm^{-1} is due to the presence of O−H in CBQDs, and D-CBQDs. Figure 6 shows comparison spectra of ADG with those of all nanocomposites. CBQD-ADG shows peaks at 2361 and 2339 cm^{-1} which are attributed to the conjugated C═C (Figure 6a), while these peaks are not so evident for NCBQDs-ADG, and SCBQDs-ADG. The peaks at 870 and 1398 cm^{-1} correspond also to C−N and S−O stretching
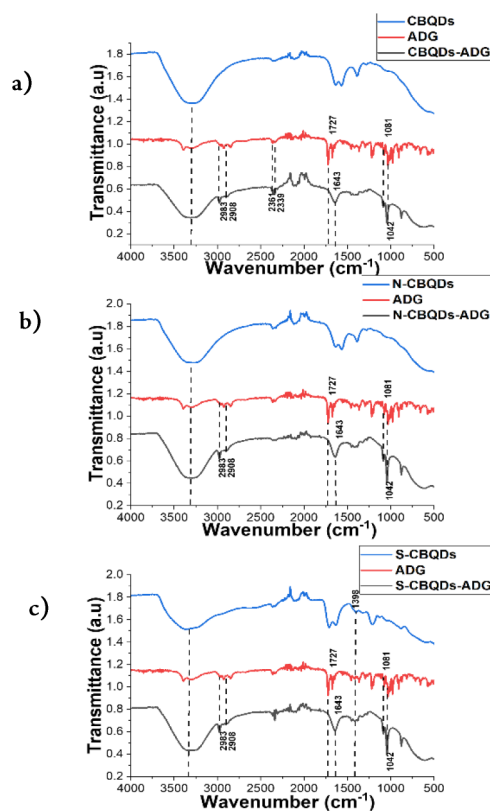

Figure 6. FT-IR comparison of (a) CBQD, ADG, and CBQD-ADG, (b) N-CBQDs, ADG, and NCBQD-ADG, and (c) S-CBQDs, ADG, and SCBQD-ADG.

vibration for NCBQD-ADG, and SCBQD-ADG, respectively (Figure 6b,c). CBQD-ADG, NCBQD-ADG, and SCBQD-ADG show peaks at 2983, 2908, 1643, 1081, and 1042 cm^{-1} due to the presence of sp^2 C−H (C−C−H), sp3 C−H (C−C−H), C=O, C−O, and C−O−C bending of the lactone ring respectively, in the molecular structure of ADG (Figure 6a−c). However, these samples show displacements in the C=O band of the coupling samples concerning pure ADG (1727 cm^{-1}). These vibrations confirm the presence of ADG molecules and support the interactions between ADG molecules and CBQDs/D-CBQDs previously confirmed in the NMR.

3. CONCLUSIONS

CBQDs, N-CBQDs, and S-CBQDs were successfully synthesized with unprecedented crystallinity. They are water-soluble, have a spherical shape, and show monodispersed distributions with diameters in the 3.1−3.4 nm range. These characteristics make them excellent candidates for use as drug delivery platforms. We synthesized and studied the nanosystems consisting of ADG conjugated to the CBQDs and D-CBQDs' surface, finding that they have a strong affinity for the aqueous phase. The log P of ADG was lowered by around 2 logarithmic units. Thereby, the carbon nanosystem hereby studied may facilitate the transport and delivery of ADG in aqueous media. The conjugated nanosystem opens the possibility of developing more effective ways of using ADG in therapeutic applications. This work could be expanded to explore the hydrophilicity improvement of other hydrophobic drugs.

4. EXPERIMENTAL SECTION

4.1. Chemicals. Citric acid (CA), 3-mercaptopropionic acid (MPA), ammonium chloride (NH$_4$Cl), sodium hydroxide (NaOH), andrographolide (ADG), deuterium oxide (D$_2$O), and 1-octanol were purchased from Sigma-Aldrich and Fisher Scientific. All glassware was rinsed with double-distilled water at least three times. All the solutions were prepared using deionized water by Aries Filter Works Gemini model GMS-105 with GMA-UV, PBS (Sigma-Aldrich), and ethanol.

4.2. Instrumentation. UV−vis absorption spectra were recorded on a Thermo Scientific Genesys 10S UV−vis spectrophotometer. Fluorescence emission and Fourier transform infrared (FTIR) spectra were obtained with a Bruker Tensor 27 Spectrofluorometer and a Bruker Tensor 27 FTIR system, respectively. NMR characterizations were performed on a Bruker Ascend Aeon 500 using deuterium oxide (D$_2$O) as solvent. The solvent signals at 4.80 and 4.81 ppm were used as internal standards for protons. In order to study the morphology and dimensions of nanocomposites, X-ray micro-analysis was recorded with a JEOL JSM-6480LV scanning electron microscope with an Evenhart Thomley secondary electron imaging (SEI) detector, an energy dispersive X-ray analysis (EDS) Genesis 2000 detector, and an FEI TALOS 200x high-resolution scanning/transmission electron microscope (TEM).

Powder diffractograms (PXRD) were collected at 300 K using a Rigaku XtaLAB SuperNova X-ray diffractometer with a microfocus Cu−Kα radiation (λ = 1.5417 Å) source and equipped with a HyPix3000 X-ray detector (50 kV, 1 mA). Powder samples were mounted on MiTeGen microloops. Powder diffractograms were collected between 6 and 60° with a step of 0.01° using the Fast phi move experiment.

4.3. Synthesis of CBQDs and Doped-CBQDs.[60] CBQDs were synthesized as reported in the literature.[61] In a typical synthesis, 2 g of citric acid was placed into a beaker and heated using a heating mantle. The solution changes from colorless to yellow and then orange. The orange color indicates the formation of CBQDs. NaOH solution is added drop by drop until the obtained orange liquid, under vigorous stirring, is neutralized at pH 7. The neutralized solution is then filtered using a syringe filter with a pore size of 0.1 μm to remove any turbostratic graphene that may have been formed as a side product. The synthesis for doped-carbon-based quantum dots (D-CBQDs) was followed as reported in the literature[62,63], where 2 g CA and MPA are pyrolyzed in a beaker with to form sulfur−carbon based quantum dots (S-CBQDs). To prepare nitrogen-doped carbon-based quantum dots (N-CBQDs) 0.8 g of citric acid is mixed with NH$_4$Cl in a beaker. The solution is heated using a hot plate, and then the mixture changes from colorless to yellow and then orange, which indicates the formation of the product. For neutralization to pH 7.00, NaOH is added drop by drop to the solution. The purification of the D-CBQDs is done through a 12 kDa dialysis bag to remove residual reagents. After the dialysis, the D-CBQDs were filtered using a syringe filter with a pore size of 0.1 μm to remove any turbostratic graphene that may have been formed as a side product.

4.4. Synthesis of CBQDs-ADG and D-CBQD-ADG Nanocomposites.[60] CBQDs-ADG and D-CBQDs (S-CBQDs and N-CBQDs)-ADG were prepared through a one-step process. CBQDs and D-CBQDs solutions between 0.3 and 0.8 absorbances (A) at 430 nm were mixed with an ethanolic solution of ADG in a volume ratio of 1:1. The nanocomposites were incubated in a sonicator at a warm temperature.

4.5. Partition Coefficient Studies. The partition coefficient measurements were done through NMR spectroscopy following the method proposed by Cumming and Rücker.[36] The partition constant and its logarithmic value (log P) are calculated from the ratio of the respective equilibrium concentrations of molecules in the two phases:

$$\log P = \log\left(\frac{C_{\text{octanol}}}{C_{\text{water}}}\right) \tag{1}$$

The method consists of dissolving an amount of the compounds in D$_2$O in an NMR tube. Then a ^{1}H NMR spectrum is taken. Afterward, an equal volume of 1-octanol is added to the NMR tube, and the phases are mixed. Then, the tube is left unperturbed to allow the phases to separate and reach equilibrium. After the equilibrium time passes, an NMR spectrum of the aqueous (lower) phase is taken. D$_2$O was used instead of water to increase andrographolide's signal due to its low solubility in H$_2$O. Finally, a characteristic of the peak of each compound is integrated within the D$_2$O peak in both spectra. The first spectrum provides RI$_w^{\text{init}}$, the second provides RI$_w^{\text{equil}}$, and K_{ow} is calculated according to eq 2:

$$K_{\text{ow}} = \frac{\text{RI}_w^{\text{init}} - \text{RI}_w^{\text{equil}}}{\text{RI}_w^{\text{equil}}} \tag{2}$$

where RI$_w^{\text{init}}$ = relative NMR signal integration of the materials in D$_2$O before equilibration with 1-octanol and RI$_w^{\text{equil}}$ = relative NMR signal integration of the materials in the aqueous phase after equilibration. The obtained K_{ow} is then utilized as

the partition constant and its logarithmic value ($\log K_{ow}$) is considered as the obtained $\log P$.

4.6. General Solubility Equation (GSE) Calculations.
Water solubility estimations were done by using the revised General Solubility Equation proposed by Jain and Yalkowsky[42].

$$\mathrm{Lg}S_w = 0.5 - 0.01(\mathrm{MP} - 25) - \log K_{ow} \qquad (3)$$

The equation solved for S_w gives the molar aqueous solubility, which we then changed to μg/mL units. The MP is the melting point of the purchased Andrographolide in degrees Celsius (231 °C) and the $\log K_{ow}$ is the partition coefficient ($\log P$). We utilized experimental $\log P$ obtained by the NMR method for the GSE calculations. $\log P$ values were obtained at a neutral pH, which increases ionization and thus reduces the $\log P$ of ADG to its $\log D$ value.[64]

■ ASSOCIATED CONTENT

⑤ Supporting Information
The Supporting Information is available free of charge at https://pubs.acs.org/doi/10.1021/acsomega.3c06252.

> In situ EDS mapping, XRD, SAED, ^{1}H and ^{13}C NMR, fluorescence, UV−vis, and FTIR spectroscopy that complements the contents of this manuscript (PDF)

■ AUTHOR INFORMATION

Corresponding Author
Nataniel Medina-Berríos − *Department of Chemistry, University of Puerto Rico, San Juan 00925-253, Puerto Rico; Molecular Sciences Research Center, University of Puerto Rico, San Juan 00925-253, Puerto Rico;* ⦿ orcid.org/0000-0002-4507-2687; Email: nataniel.medina@upr.edu

Authors
Wenndy Pantoja-Romero − *Department of Chemistry, University of Puerto Rico, San Juan 00925-253, Puerto Rico; Molecular Sciences Research Center, University of Puerto Rico, San Juan 00925-253, Puerto Rico*

Alexis Lavín Flores − *Department of Chemistry, University of Puerto Rico, San Juan 00925-253, Puerto Rico; Molecular Sciences Research Center, University of Puerto Rico, San Juan 00925-253, Puerto Rico*

Sebastián C. Díaz Vélez − *Department of Chemistry, University of Puerto Rico, San Juan 00925-253, Puerto Rico; Molecular Sciences Research Center, University of Puerto Rico, San Juan 00925-253, Puerto Rico*

Anna C. Martínez Guadalupe − *Molecular Sciences Research Center, University of Puerto Rico, San Juan 00925-253, Puerto Rico; Department of Biology, University of Puerto Rico, San Juan 00925-253, Puerto Rico*

Mariana T. Torres Mulero − *Molecular Sciences Research Center, University of Puerto Rico, San Juan 00925-253, Puerto Rico; Department of Biology, University of Puerto Rico, San Juan 00925-253, Puerto Rico*

Kim Kisslinger − *Brookhaven National Lab, Upton, New York 11973, United States*

Magaly Martínez-Ferrer − *Division of Cancer Biology, University of Puerto Rico Comprehensive Cancer Center, San Juan 00936-3027, Puerto Rico; Department of Pharmaceutical Sciences, School of Pharmacy, University of Puerto Rico San Juan 00925-253, Puerto Rico*

Gerardo Morell − *Molecular Sciences Research Center, University of Puerto Rico, San Juan 00925-253, Puerto Rico;*

Department of Physics, University of Puerto Rico, San Juan 00925-253, Puerto Rico

Brad R. Weiner − *Department of Chemistry, University of Puerto Rico, San Juan 00925-253, Puerto Rico; Molecular Sciences Research Center, University of Puerto Rico, San Juan 00925-253, Puerto Rico*

Complete contact information is available at:
https://pubs.acs.org/10.1021/acsomega.3c06252

Author Contributions
N.M.-B. & W.P.-R.: data curation, formal analysis, investigation, methodology, project administration, validation, visualization, writing original draft and writing-review and editing. A.L.F.: data curation, formal analysis, validation, visualization, writing original draft and writing-review and editing. S.C.D.V.: data curation, formal analysis, investigation, visualization and writing original draft. A.C.M.G.: data curation, formal analysis, investigation, visualization and writing original draft. M.T.T.M.: data curation, formal analysis, investigation, visualization and writing original draft. K.K.: data curation, investigation. G.M.: funding acquisition, resources, supervision, validation, visualization, and writing-review and editing. B.R.W.: funding acquisition, resources, supervision, validation, visualization, and writing-review and editing. N.M.-B. and W.P.-R. contributed equally to this work.

Notes

■ ACKNOWLEDGMENTS

■ REFERENCES

(1) Soo, H. L.; Quah, S. Y.; Sulaiman, I.; Sagineedu, S. R.; Lim, J. C. W.; Stanslas, J. Advances and Challenges in Developing Andrapholide and Its Analogues as Cancer Therapeutic Agents. *Drug Discovery Today* **2019**, 24 (9), 1890−1898.

(2) Dai, X.; Zhang, J.; Arfuso, F.; Chinnathambi, A.; Zayed, M. E.; Alharbi, S. A.; Kumar, A. P.; Ahn, K. S.; Sethi, G. Targeting TNF-Related Apoptosis-Inducing Ligand (TRAIL) Receptor by Natural Products as a Potential Therapeutic Approach for Cancer Therapy. *Exp Biol. Med. (Maywood)* **2015**, 240 (6), 760−773.

(3) Wei, R.-J.; Zhang, X.-S.; He, D.-L. Andrographolide Sensitizes Prostate Cancer Cells to TRAIL-Induced Apoptosis. *Asian J. Androl* **2018**, 20 (2), 200−204.

(4) Zeng, Q.; Ou, L.; Zhao, G.; Cai, P.; Liao, Z.; Dong, W.; Liang, X. Preparation and Characterization of PEG4000 Palmitate/PEG8000 Palmitate-Solid Dispersion Containing the Poorly Water-Soluble Drug Andrographolide. *Advances in Polymer Technology* **2020**, 2020, 1−7.

(5) Gary, Price; Patel, D. *Drug Bioavailability*; StatPearls Publishing. https://www.ncbi.nlm.nih.gov/books/NBK557852/.

(6) Chen, H.-W.; Huang, C.-S.; Li, C.-C.; Lin, A.-H.; Huang, Y.-J.; Wang, T.-S.; Yao, H.-T.; Lii, C.-K. Bioavailability of Andrographolide and Protection against Carbon Tetrachloride-Induced Oxidative Damage in Rats. *Toxicol. Appl. Pharmacol.* **2014**, 280 (1), 1−9.

(7) Ye, L.; Wang, T.; Tang, L.; Liu, W.; Yang, Z.; Zhou, J.; Zheng, Z.; Cai, Z.; Hu, M.; Liu, Z. Poor Oral Bioavailability of a Promising

Anticancer Agent Andrographolide Is Due to Extensive Metabolism and Efflux by P-glycoprotein. *J. Pharm. Sci.* **2011**, *100* (11), 5007−5017.

(8) Kansom, T.; Sajomsang, W.; Saeeng, R.; Charoensuksai, P.; Opanasopit, P.; Tonglairoum, P. Apoptosis Induction and Antimigratory Activity of Andrographolide Analog (3A.1)-Incorporated Self-Assembled Nanoparticles in Cancer Cells. *AAPS PharmSciTech* **2018**, *19* (7), 3123−3133.

(9) Liu, W.; Cheng, M.; Yuan, F.; He, J.; Feng, Y.; Jin, Y.; Feng, J.; Yang, S.; Tu, L. Enhancing Oral Bioavailability of Andrographolide via Sodium Dodecyl Sulfate and D-α-Tocopherol Polyethylene Glycol 1000 Succinate Copolymer Modified Nanocrystals. *Journal of Drug Delivery Science and Technology* **2023**, *79*, No. 104006.

(10) Pingle, P.; Mourya, A.; Namdeo, M.; Babu, K. C.; Veerabomma, H.; Maurya, R.; Singh, P. K.; Mehra, N. K.; Srivastava, S.; Madan, J. Andrographolide-Soya-L-α-Phosphatidyl Choline Complex Augmented Solubility and Drug Delivery in Leishmania Donovani, a Causative Agent for Cutaneous and Visceral Leishmaniasis. *AAPS PharmSciTech* **2023**, *24* (1), 46.

(11) Rahul, M.; Boini, T.; Lakshminarayana, M.; Radhakrishnan, T.; Kolangarakalam Sudayadas, R. Approaches to Improve Solubility, Stability and the Clinical Potential of Andrographolide: A Review. *JYP* **2022**, *14* (1), 15−20.

(12) Tao Gong, T. G.; Ke Ren, K. R.; Zhirong Zhang, Z. Z.; et al. Physicochemical Characteristics and Oral Bioavailability of Andrographolide Complexed with Hydroxypropyl-ß-Cyclodextrin. *Pharmazie* **2009**, *8*, 515−520.

(13) Drug Delivery Systems. In *Strategies to Modify the Drug Release from Pharmaceutical Systems*; Elsevier, 2015; pp 87−194.

(14) Du, H.; Yang, X.; Li, H.; Han, L.; Li, X.; Dong, X.; Zhu, Q.; Ye, M.; Feng, Q.; Niu, X. Preparation and Evaluation of Andrographolide-Loaded Microemulsion. *J. Microencapsulation* **2012**, *29* (7), 657−665.

(15) Yao, Y.; Zhou, Y.; Liu, L.; Xu, Y.; Chen, Q.; Wang, Y.; Wu, S.; Deng, Y.; Zhang, J.; Shao, A. Nanoparticle-Based Drug Delivery in Cancer Therapy and Its Role in Overcoming Drug Resistance. *Front. Mol. Biosci.* **2020**, *7*, 193.

(16) Liu, H.; Qiu, J.; Zhang, R.; Li, J.; Sang, Y.; Tang, W.; Rivera Gil, P. Fluorescent Graphene Quantum Dots as Traceable, pH-Sensitive Drug Delivery Systems. *IJN* **2015**, 6709.

(17) Li, K.; Zhao, X.; Wei, G.; Su, Z. Recent Advances in the Cancer Bioimaging with Graphene Quantum Dots. *CMC* **2018**, *25* (25), 2876−2893.

(18) Prabhu, S. A.; Kavithayeni, V.; Suganthy, R.; Geetha, K. Graphene Quantum Dots Synthesis and Energy Application: A Review. *Carbon Lett.* **2021**, *31*, 1.

(19) Kim, S.; Hwang, S. W.; Kim, M.-K.; Shin, D. Y.; Shin, D. H.; Kim, C. O.; Yang, S. B.; Park, J. H.; Hwang, E.; Choi, S.-H.; Ko, G.; Sim, S.; Sone, C.; Choi, H. J.; Bae, S.; Hong, B. H. Anomalous Behaviors of Visible Luminescence from Graphene Quantum Dots: Interplay between Size and Shape. *ACS Nano* **2012**, *6* (9), 8203−8208.

(20) Tian, P.; Tang, L.; Teng, K. S.; Lau, S. P. Graphene Quantum Dots from Chemistry to Applications. *Materials Today Chemistry* **2018**, *10*, 221−258.

(21) Zhao, C.; Song, X.; Liu, Y.; Fu, Y.; Ye, L.; Wang, N.; Wang, F.; Li, L.; Mohammadniaei, M.; Zhang, M.; Zhang, Q.; Liu, J. Synthesis of Graphene Quantum Dots and Their Applications in Drug Delivery. *J. Nanobiotechnol* **2020**, *18* (1), 142.

(22) Tabish, T. A.; Scotton, C. J.; Ferguson, D. C. J.; Lin, L.; van der Veen, A.; Lowry, S.; Ali, M.; Jabeen, F.; Ali, M.; Winyard, P. G.; Zhang, S. Biocompatibility and Toxicity of Graphene Quantum Dots for Potential Application in Photodynamic Therapy. *Nanomedicine* **2018**, *13* (15), 1923−1937.

(23) D'souza, S. L.; Deshmukh, B.; Bhamore, J. R.; Rawat, K. A.; Lenka, N.; Kailasa, S. K. Synthesis of Fluorescent Nitrogen-Doped Carbon Dots from Dried Shrimps for Cell Imaging and Boldine Drug Delivery System. *RSC Adv.* **2016**, *6* (15), 12169−12179.

(24) Ding, H.; Du, F.; Liu, P.; Chen, Z.; Shen, J. DNA−Carbon Dots Function as Fluorescent Vehicles for Drug Delivery. *ACS Appl. Mater. Interfaces* **2015**, *7* (12), 6889−6897.

(25) Feng, T.; Ai, X.; An, G.; Yang, P.; Zhao, Y. Charge-Convertible Carbon Dots for Imaging-Guided Drug Delivery with Enhanced *in Vivo* Cancer Therapeutic Efficiency. *ACS Nano* **2016**, *10* (4), 4410−4420.

(26) Feng, T.; Ai, X.; Ong, H.; Zhao, Y. Dual-Responsive Carbon Dots for Tumor Extracellular Microenvironment Triggered Targeting and Enhanced Anticancer Drug Delivery. *ACS Appl. Mater. Interfaces* **2016**, *8* (29), 18732−18740.

(27) Kou, X.; Jiang, S.; Park, S.-J.; Meng, L.-Y. A Review: Recent Advances in Preparations and Applications of Heteroatom-Doped Carbon Quantum Dots. *Dalton Trans.* **2020**, *49* (21), 6915−6938.

(28) Neubeck, S.; Ponomarenko, L. A.; Freitag, F.; Giesbers, A. J. M.; Zeitler, U.; Morozov, S. V.; Blake, P.; Geim, A. K.; Novoselov, K. S. From One Electron to One Hole: Quasiparticle Counting in Graphene Quantum Dots Determined by Electrochemical and Plasma Etching. *Small* **2010**, *6* (14), 1469−1473.

(29) Sawy, A. M.; Barhoum, A.; Abdel Gaber, S. A.; El-Hallouty, S. M.; Shousha, W. G.; Maarouf, A. A.; Khalil, A. S. G. Insights of Doxorubicin Loaded Graphene Quantum Dots: Synthesis, DFT Drug Interactions, and Cytotoxicity. *Materials Science and Engineering: C* **2021**, *122*, No. 111921.

(30) Xue, Z.; Sun, Q.; Zhang, L.; Kang, Z.; Liang, L.; Wang, Q.; Shen, J.-W. Graphene Quantum Dot Assisted Translocation of Drugs into a Cell Membrane. *Nanoscale* **2019**, *11* (10), 4503−4514.

(31) Kah, M.; Brown, C. D. LogD: Lipophilicity for Ionisable Compounds. *Chemosphere* **2008**, *72* (10), 1401−1408.

(32) Amézqueta, S.; Subirats, X.; Fuguet, E.; Rosés, M.; Ràfols, C. Octanol-Water Partition Constant. In *Liquid-Phase Extraction*; Elsevier, 2020; pp 183−208.

(33) Pandey, G.; Rao, C. Andrographolide: Its Pharmacology, Natural Bioavailability and Current Approaches to Increase Its Content in Andrographispaniculata. *Int. J. Complement Alt. Med.* **2018**, *11* (4), 355 DOI: 10.15406/ijcam.2018.11.00425.

(34) Schulte, B.; König, M.; Escher, B. I.; Wittenburg, S.; Proj, M.; Wolf, V.; Lemke, C.; Schnakenburg, G.; Sosič, I.; Streeck, H.; Müller, C. E.; Gütschow, M.; Steinebach, C. Andrographolide Derivatives Target the KEAP1/NRF2 Axis and Possess Potent Anti-SARS-CoV-2 Activity. *ChemMedChem* **2022**, *17* (5), No. 2100732, DOI: 10.1002/cmdc.202100732.

(35) Fielding, L. Determination of Association Constants (Ka) from Solution NMR Data. *Tetrahedron* **2000**, *56* (34), 6151−6170.

(36) Cumming, H.; Rücker, C. Octanol−Water Partition Coefficient Measurement by a Simple ^{1}H NMR Method. *ACS Omega* **2017**, *2* (9), 6244−6249.

(37) Barthel, C.; Massiot, G.; Lavaud, C. An Easy-to-use and General Nuclear Magnetic Resonance Method for the Determination of Partition Coefficients of Drugs and Natural Products. *Magn. Reson. Chem.* **2021**, *59* (8), 835−843.

(38) Chellampillai, B.; Pawar, A. P. Improved Bioavailability of Orally Administered Andrographolide from pH-Sensitive Nanoparticles. *Eur. J. Drug Metab Pharmacokinet* **2011**, *35* (3−4), 123−129.

(39) Li, H.; Qu, X.; Qian, W.; Song, Y.; Wang, C.; Liu, W. Andrographolide-loaded Solid Lipid Nanoparticles Enhance Anticancer Activity against Head and Neck Cancer and Precancerous Cells. *Oral Diseases* **2022**, *28* (1), 142−149.

(40) Guccione, C.; Oufir, M.; Piazzini, V.; Eigenmann, D. E.; Jähne, E. A.; Zabela, V.; Faleschini, M. T.; Bergonzi, M. C.; Smiesko, M.; Hamburger, M.; Bilia, A. R. Andrographolide-Loaded Nanoparticles for Brain Delivery: Formulation, Characterisation and in Vitro Permeability Using hCMEC/D3 Cell Line. *Eur. J. Pharm. Biopharm.* **2017**, *119*, 253−263.

(41) Yao, S.; Chen, N.; Sun, X.; Wang, Q.; Li, M.; Chen, Y. Size-Dependence of the Skin Penetration of Andrographolide Nanosuspensions: In Vitro Release-Ex Vivo Permeation Correlation and

Visualization of the Delivery Pathway. *Int. J. Pharm.* **2023**, *641*, No. 123065.

(42) Ran, Y.; He, Y.; Yang, G.; Johnson, J. L. H.; Yalkowsky, S. H. Estimation of Aqueous Solubility of Organic Compounds by Using the General Solubility Equation. *Chemosphere* **2002**, *48* (5), 487−509.

(43) Naik, J. P.; Sutradhar, P.; Saha, M. Molecular Scale Rapid Synthesis of Graphene Quantum Dots (GQDs). *J. Nanostruct Chem.* **2017**, *7* (1), 85−89.

(44) Sun, Y.; Wang, S.; Li, C.; Luo, P.; Tao, L.; Wei, Y.; Shi, G. Large Scale Preparation of Graphene Quantum Dots from Graphite with Tunable Fluorescence Properties. *Phys. Chem. Chem. Phys.* **2013**, *15* (24), 9907.

(45) Fayos, J. Possible 3D Carbon Structures as Progressive Intermediates in Graphite to Diamond Phase Transition. *J. Solid State Chem.* **1999**, *148* (2), 278−285.

(46) Raccichini, R.; Varzi, A.; Chakravadhanula, V. S. K.; Kübel, C.; Balducci, A.; Passerini, S. Enhanced Low-Temperature Lithium Storage Performance of Multilayer Graphene Made through an Improved Ionic Liquid-Assisted Synthesis. *J. Power Sources* **2015**, *281*, 318−325.

(47) He, P.; Yang, S.; Liu, X.; Yang, Y.; Zheng, J.; Liu, X.; Xu, B. Highly Stable Yellow-Emitting Fluorescent Film Based on Graphene Quantum Dots for White Laser-Emitting Devices. *J. Lumin.* **2021**, *238*, No. 118275.

(48) Barbarella, G.; Dembech, P.; Garbesi, A.; Fava, A. 13C NMR of Organosulphur Compounds: I—the Effects of Sulphur Substituents on the13C Chemical Shifts of Alkyl Chains and of S-Heterocycles. *Org. Magn. Reson.* **1976**, *8* (2), 108−114.

(49) Still, I. W. J.; Plavac, N.; McKinnon, D. M.; Chauhan, M. S. Carbon-13 Nuclear Magnetic Resonance Spectra of Organic Sulfur Compounds. Comparison of Chemical Shifts for Carbonyl and Thiocarbonyl Compounds in the Pyrone, Thiopyrone, and Pyridone Series. *Can. J. Chem.* **1976**, *54* (2), 280−289.

(50) Chen, S.; Hai, X.; Xia, C.; Chen, X.-W.; Wang, J.-H. Preparation of Excitation-Independent Photoluminescent Graphene Quantum Dots with Visible-Light Excitation/Emission for Cell Imaging. *Chem. − Eur. J.* **2013**, *19* (47), 15918−15923.

(51) Li, B.; Wang, Y.; Huang, L.; Qu, H.; Han, Z.; Wang, Y.; Kipper, M. J.; Belfiore, L. A.; Tang, J. Review of Performance Improvement Strategies for Doped Graphene Quantum Dots for Fluorescence-Based Sensing. *Synth. Met.* **2021**, *276*, No. 116758.

(52) Liu, Y.; Xu, X.; Lv, S.; Li, H.; Si, Z.; Wu, X.; Ran, R.; Weng, D. Nitrogen Doped Graphene Quantum Dots as a Cocatalyst of SrTiO$_3$ (Al)/CoO$_x$ for Photocatalytic Overall Water Splitting. *Catal. Sci. Technol.* **2021**, *11* (9), 3039−3046.

(53) Arcudi, F.; Đorđević, L.; Prato, M. Synthesis, Separation, and Characterization of Small and Highly Fluorescent Nitrogen-Doped Carbon NanoDots. *Angew. Chem., Int. Ed.* **2016**, *55* (6), 2107−2112.

(54) Yen, C.-C.; Chen, Y.-C.; Wu, M.-T.; Wang, C.-C.; Wu, Y.-T. Nanoemulsion as a Strategy for Improving the Oral Bioavailability and Anti-Inflammatory Activity of Andrographolide. *IJN* **2018**, *13*, 669−680.

(55) Yang, F.; Bao, W.; Liu, T.; Zhang, B.; Huang, S.; Yang, W.; Li, Y.; Li, N.; Wang, C.; Pan, C.; Li, Y. Nitrogen-Doped Graphene Quantum Dots Prepared by Electrolysis of Nitrogen-Doped Nano-mesh Graphene for the Fluorometric Determination of Ferric Ions. *Microchim Acta* **2020**, *187* (6), 322.

(56) Kadian, S.; Manik, G. Sulfur Doped Graphene Quantum Dots as a Potential Sensitive Fluorescent Probe for the Detection of Quercetin. *Food Chem.* **2020**, *317*, No. 126457.

(57) Tabish, T. A.; Zhang, S. Graphene Quantum Dots: Syntheses, Properties, and Biological Applications. In *Comprehensive Nanoscience and Nanotechnology*; Elsevier, 2016; pp 171−192.

(58) Gu, J.; Zhang, X.; Pang, A.; Yang, J. Facile Synthesis and Photoluminescence Characteristics of Blue-Emitting Nitrogen-Doped Graphene Quantum Dots. *Nanotechnology* **2016**, *27* (16), No. 165704.

(59) Ngoc Anh, N. T.; Chang, P.-Y.; Doong, R.-A. Sulfur-Doped Graphene Quantum Dot-Based Paper Sensor for Highly Sensitive and Selective Detection of 4-Nitrophenol in Contaminated Water and Wastewater. *RSC Adv.* **2019**, *9* (46), 26588−26597.

(60) Medina-Berríos, N.; Pantoja, W.; Lavin, A.; M., Martínez-Ferrer; Weiner, B. R.; Morell, G. A New Delivery Agent for Hydrophobic Drugs. 63/492,024.

(61) Dong, Y.; Shao, J.; Chen, C.; Li, H.; Wang, R.; Chi, Y.; Lin, X.; Chen, G. Blue Luminescent Graphene Quantum Dots and Graphene Oxide Prepared by Tuning the Carbonization Degree of Citric Acid. *Carbon* **2012**, *50* (12), 4738−4743.

(62) Anh, N. T. N.; Doong, R. One-Step Synthesis of Size-Tunable Gold@Sulfur-Doped Graphene Quantum Dot Nanocomposites for Highly Selective and Sensitive Detection of Nanomolar 4-Nitrophenol in Aqueous Solutions with Complex Matrix. *ACS Appl. Nano Mater.* **2018**, *1* (5), 2153−2163.

(63) Rao, Z.; Geng, F.; Zhou, Y.; Cao, D.; Kang, Y. N-Doped Graphene Quantum Dots as a Novel Highly-Efficient Matrix for the Analysis of Perfluoroalkyl Sulfonates and Other Small Molecules by MALDI-TOF MS. *Anal. Methods* **2017**, *9* (13), 2014−2020.

(64) Hill, A. P.; Young, R. J. Getting Physical in Drug Discovery: A Contemporary Perspective on Solubility and Hydrophobicity. *Drug Discovery Today* **2010**, *15* (15−16), 648−655.